# First Measurements of Fuel-Ablator Interface Instability Growth in Inertial Confinement Fusion Implosions on the National Ignition Facility

C. R. Weber,[1] T. Döppner,[1] D. T. Casey,[1] T. L. Bunn,[1] L. C. Carlson,[2] R. J. Dylla-Spears,[1] B. J. Kozioziemski,[1] A. G. MacPhee,[1] A. Nikroo,[1,2] H. F. Robey,[1] J. D. Sater,[1] and V. A. Smalyuk[1]
[1]*Lawrence Livermore National Laboratory, Livermore, California 94550, USA*
[2]*General Atomics, San Diego, California 92121, USA*

(Received 8 February 2016; revised manuscript received 21 June 2016; published 9 August 2016)

Direct measurements of hydrodynamic instability growth at the fuel-ablator interface in inertial confinement fusion (ICF) implosions are reported for the first time. These experiments investigate one of the degradation mechanisms behind the lower-than-expected performance of early ICF implosions on the National Ignition Facility. Face-on x-ray radiography is used to measure instability growth occurring between the deuterium-tritium fuel and the plastic ablator from well-characterized perturbations. This growth starts in two ways through separate experiments—either from a preimposed interface modulation or from ablation front feedthrough. These experiments are consistent with analytic modeling and radiation-hydrodynamic simulations, which say that a moderately unstable Atwood number and convergence effects are causing in-flight perturbation growth at the interface. The analysis suggests that feedthrough from outersurface perturbations dominates the interface perturbation growth at mode 60.

DOI: 10.1103/PhysRevLett.117.075002

Understanding and mitigating the hydrodynamic instability growth occurring during the implosion of an inertial confinement fusion (ICF) capsule is essential to achieving the desired fusion performance and ultimately achieving ignition with ICF. In the indirect drive configuration used at the National Ignition Facility (NIF) [1] laser beams irradiate the inside of a high-$Z$ (Au or U) hohlraum, where their energy is converted into soft x rays. The x-ray environment inside the hohlraum heats and ablates the capsule, sending a series of carefully timed shock waves inwards and compressing it to 30–40× smaller than its initial radius. This compression process generates hydrodynamic instabilities on the ablation front of the capsule through the ablative Rayleigh-Taylor (RT) instability [2,3] and on the interface between the deuterium-tritium (DT) fuel and the ablator through the classical RT and Richtmyer-Meshkov (RM) instabilities [3].

Initially the interface is stable to the RT instability, but instability can arise from high-energy x rays heating the ablator near the interface and lowering its density below that of the fuel, causing an unstable Atwood number [$A = (\rho_1 - \rho_2)/(\rho_1 + \rho_2)$, where $\rho$ is the density]. ICF capsule designs attempt to control the Atwood number by shielding the interface with high-$Z$ dopant added to the ablator [4,5]. Yet experiments during the National Ignition Campaign (NIC) (2009–2012) [6] observed significant mixing of ablator material into the hot spot [7,8], while subsequent experiments [9,10] have shown improvements by modifying the laser pulse to improve hydrodynamic stability. This implies that either instability growth is greater than originally modeled or perturbation seeds are not adequately known [11].

To better understand instability growth in these ICF implosions, a series of experiments measuring the growth of preimposed perturbations has been undertaken [16–19]. Thus far, good agreement between simulations and the observed growth has been found at several mode numbers and using several pulse shapes [20]. These HGR measurements were made using a perturbation seeded on the outside of the capsule and measuring its growth on the ablation front. Here we report on the first experiments directly measuring the growth of a perturbation on the interface between the DT fuel and the ablator.

The setup for these experiments is shown in Fig. 1. The capsule is placed on an Au cone, centering it within the Au hohlraum. Of the NIF's 192 laser beams, 184 are directed into the hohlraum, with the remaining eight laser beams pointed towards a Sc backlighter, creating 4.3 keV x rays. The backlighter x rays pass down the axis of the cone, through half of the capsule, out a high-density carbon window in the wall of the hohlraum, through a 12 $\mu$m wide slit, and finally are recorded by the GXD [21] at 12× magnification. The GXD records images at four times as the capsule is imploding. Through this process modulations in the capsule's optical depth (OD $= \int \kappa\rho\, dr$, where $\kappa$ is the opacity) can be measured.

This setup has been used in past HGR experiments, but these are the first to include a DT ice layer. This ice layer can be seen in the initial condition radiograph of Fig. 1(b). The experiment shown here had sinusoidal ripples machined on the interface between the ice and the ablator. The design for these experiments is based on the "low-foot" laser pulse and capsules [22] used during the NIC but was scaled down by 0.8× in order to operate at reduced laser

 

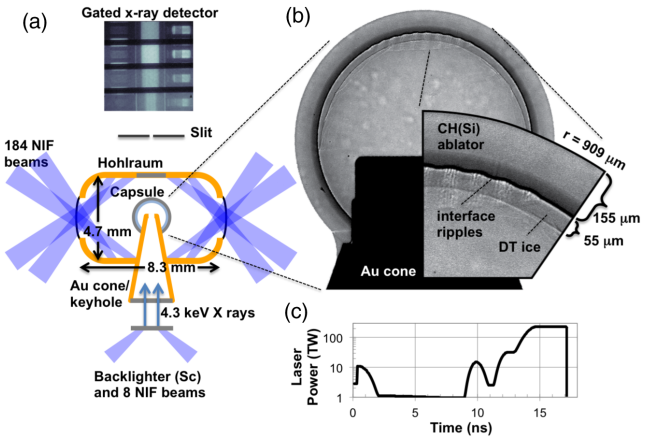


FIG. 1. (a) Experimental setup for the layered hydrogrowth radiography (HGR) platform. An Au cone enters through the hohlraum and the capsule, allowing backlighter x rays to pass through half of the capsule and be recorded by the gated x-ray detector (GXD). (b) The capsule has a Si-doped plastic (CH) ablator with an inner DT ice layer. The experiment shown here includes mode 60 perturbations between the ablator and the ice, visible in the zoomed-in image. (c) The laser pulse uses four shocks and reaches 230 TW peak power with 0.9 MJ of total energy.

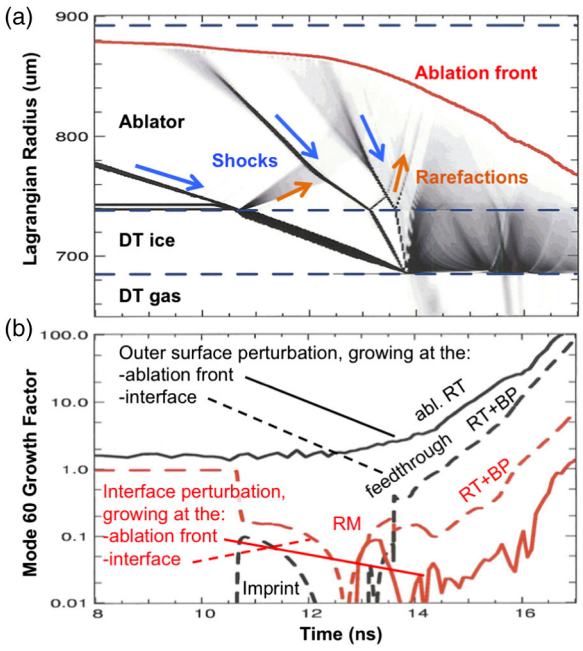


FIG. 2. (a) Shock trajectories, produced by plotting the logarithmic derivative of the pressure, plotted in Lagrangian coordinates. Shocks are timed to merge near the DT ice-gas boundary. (b) The feedthrough between the ablation front and fuel-ablator interface is shown through growth factors (normalized amplitudes) from a mode 60 outersurface perturbation (black) and an interface perturbation (red) growing at the ablation front (solid) or the interface (dashed).

energy (and facility cost) but be hydrodynamically equivalent. The laser pulse, shown in Fig. 1(c), has 0.9 MJ of energy and a peak power of 230 TW. The capsule is 909 $\mu$m in outer radius with a 155 $\mu$m thick plastic (CH) ablator and a DT ice layer that is 55 $\mu$m thick in the field of view [23]. The ablator contains graded silicon dopant of up to 2.3% to block high-energy x-ray preheat.

Instability growth at the fuel-ablator interface can originate either from a local perturbation at this interface or from a perturbation that imprints from the ablation front [24–30]. These experiments address both scenarios. The dynamics of these interactions are displayed in Fig. 2 from one-dimensional and two-dimensional HYDRA simulations [31]. In Fig. 2(a), the shocks launched by this four-shock pulse [Fig. 1(c)] are shown by plotting the logarithmic gradient of pressure in Lagrangian coordinates (i.e., initial mass coordinates). The first shock reaches the interface between the ice and the ablator at 10.6 ns, with subsequent shocks arriving at 13.1 and 13.6 ns (the fourth shock does not appear pronounced in this view). Figure 2(b) shows normalized perturbation amplitudes at the ablation front (solid) or fuel-ablator interface (dashed) of a mode 60 perturbation seeded at either the outer surface (black) or the interface (red). The shocks launched from the ablation front carry their perturbation and imprint on the interface with an amplitude $\eta_{\text{imprint}}/\eta_0 = \sin(kc_st)/kc_st$, where $k = l/R$ is the wave number, $l$ is the spherical mode number, and $c_s$ is the sound speed (here $\eta_{\text{imprint}}/\eta_0 \approx 0.1$; black dashed line at 10.6 ns). The perturbation at this interface grows through the RM instability, which causes oscillations in the amplitude as each shock drives a phase inversion. Feedthrough of ablation front growth onto the interface due to their proximity is also a large component of interfacial perturbation growth. This factor is approximately $\eta_{\text{feedthrough}} \approx \eta_{\text{abl}} e^{-l\Delta R/R}$ and reaches a maximum for mode 60 of $\eta_{\text{feedthrough}} \approx 0.13\eta_{\text{abl}}$ before the rarefaction decompresses the capsule around 14 ns.

Perturbations on the fuel-ablator interface experience classical RM growth from each of the four shock waves, inducing linear growth at a rate of $\dot{\eta}_{\text{RM}} = \eta_0 A\delta\dot{R}l/R$, where $\delta\dot{R}$ is the impulsive interface velocity jump. At 10.5 ns the interface perturbation compresses from the first shock wave, inverts phase, and then grows in amplitude. Preheat and acceleration of the interface can lead to classical RT growth of $\eta_{\text{RT}}/\eta_0 = \exp\int \gamma_{\text{RT}} dt$ where $\gamma_{\text{RT}} = \sqrt{A\ddot{R}l/R}$. The spherical geometry and radial velocity can amplify the interface amplitude through Bell-Plesset (BP) effects [32–34], inducing growth of the form $\eta_{\text{RT+BP}}/\eta_0 = (R_0/R)^{3/2} \exp\int \sqrt{\gamma^2_{\text{RT-like}} + \gamma^2_R} dt$, where $\gamma_R = 3/4(\dot{R}/R)^2$ and $\gamma_{\text{RT-like}} \approx \gamma_{\text{RT}}$. These effects act on interface perturbations that are initially present or that arise from ablation front imprint and feedthrough.

These two methods of generating an interface perturbation (ablation front imprint or initial interface seed) are used here in separate experiments. The first method uses side-by-side mode 60/90 perturbations on the outside of the

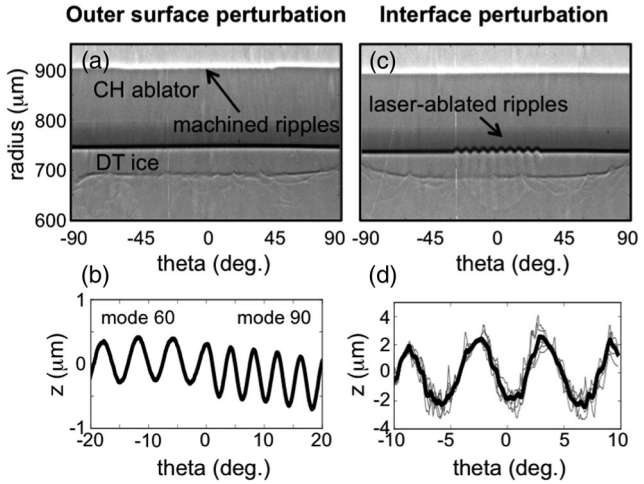


FIG. 3. [(a) and (b)] Images of the capsule and ice layer, unrolled into radius vs theta, for the (a) outersurface perturbation experiment and (b) interface perturbation experiment. The perturbation lineouts are shown in (c) and (d), respectively. The outersurface perturbation included both modes 60 and 90, with an amplitude of 0.35 $\mu$m. The interface perturbation only used mode 60 with an amplitude of 4.4 $\mu$m. In (d), the average profile is shown as a thick line and individual lineouts are shown as thin grey lines, showing mode ~500 structure present from the laser ablation process that made this interface perturbation.

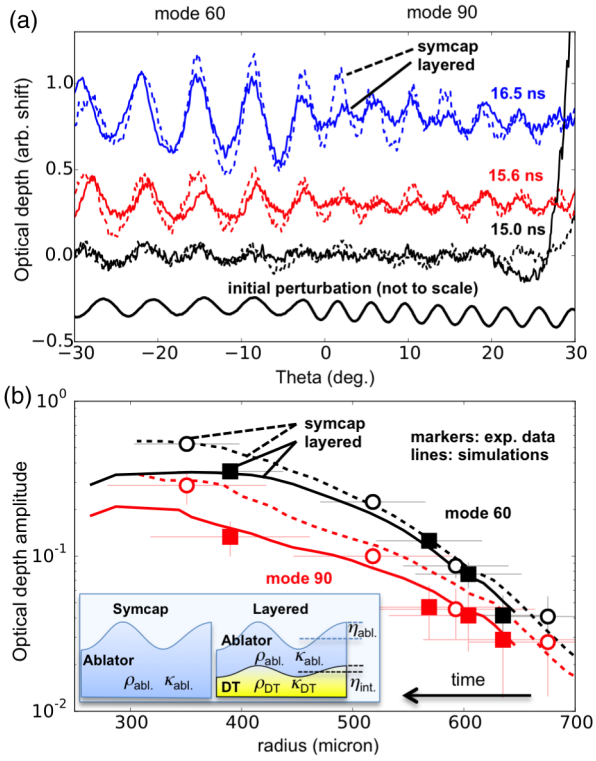


FIG. 4. Results from the outersurface perturbation experiment. (a) Radiograph lineouts converted to optical depth. The symcap experiment (N140914) is shown as dashed lines and the layered experiment (N141026) is shown as solid lines. The initial perturbation is shown at the bottom. (b) Single mode amplitudes from both experiments after correcting for the transfer function of the imaging system. Experimental data are shown as markers and postshot simulations are shown as lines. The inset shows a model of the two experiments, describing their density, $\rho$, opacity, $\kappa$, and perturbation amplitude, $\eta$.

ablator. This same perturbation is placed on two capsules for comparison, a DT-layered capsule and a symcap (a capsule with the DT replaced with the equivalent mass of 10 $\mu$m of additional ablator material) through a lathe technique used in past HGR experiments. The layered capsule is shown in Fig. 3(a) (with the image unrolled into radius vs azimuthal angle). The 0.35 $\mu$m amplitude perturbations on the outer surface are faintly visible. These perturbations are characterized through atomic-force microscopy and a lineout is shown in Fig. 3(b).

In the second layered experiment, a perturbation is machined directly on the inner ablator surface, between the DT ice and the CH plastic. This perturbation was imposed through a new technique using laser ablation [35]. After the hole for the Au cone was cut into the capsule, a UV laser was used to remove individual spots to create a sinusoidal mode 60 pattern. This technique also left higher-mode features the size of the laser spot (mode ~500). This target is shown in Figs. 1(b) and 3(c). The perturbation is characterized using a Leica confocal microscope [35] and is shown in Fig. 3(d).

Results from the outersurface perturbation experiments are shown in Fig. 4(a). The transmission signal was processed by removing the background signal, dividing by the backlighter profile, and converting to optical depth. Here the width of the data was converted to angle around the capsule by detecting the center of convergence between the various times. The data also show that mode 60 is growing $2-3\times$ larger than mode 90. As previous experiments have shown, this is because higher modes have more ablative stabilization and mode 90 is close to the zero-growth node caused by phase oscillations in the shock wave (predicted to occur at mode 110 for this capsule and laser pulse) [20,36]. The data also show that the amplitude between the symcap (dashed) and layered capsule (solid) is similar at the earliest time, but the symcap amplitude appears to grow larger later in time. The single mode amplitudes from these experiments are shown in Fig. 4(b) and compared with two-dimensional postshot simulations using HYDRA [37]. Good agreement is found between the simulations and the data, with the simulation falling within the error bars of most data points.

The larger observed modulations on the symcap appear to be due to the opacity difference between the ablator and fuel and not because of larger amplitudes. Simulations suggest that the scenario inset in Fig. 4(b) is occurring, with the same areal density modulations and ablation front amplitudes but differences in OD due to the fuel. From this model the measured OD amplitude is $\Delta \mathrm{OD}_{\mathrm{layered}} = \eta_{\mathrm{int}}\rho_{\mathrm{DT}}\kappa_{\mathrm{DT}} + \eta_{\mathrm{abl}}\rho_{\mathrm{abl}}\kappa_{\mathrm{abl}} - \eta_{\mathrm{int}}\rho_{\mathrm{abl}}\kappa_{\mathrm{abl}}$. Since

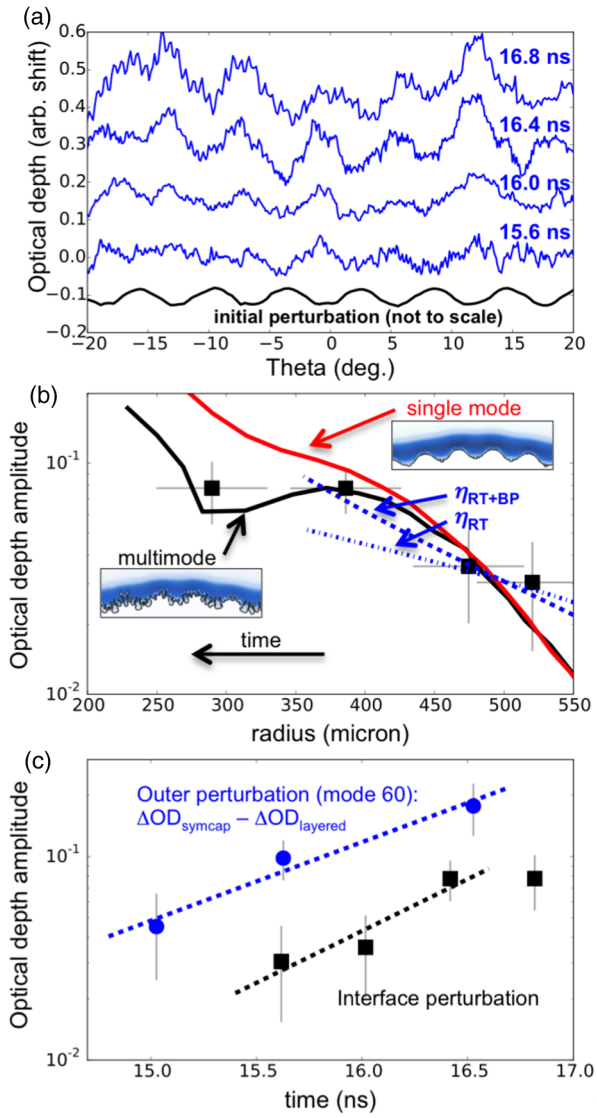


FIG. 5. Results from the interface perturbation experiment (N150305). (a) Radiograph results converted to optical depth. The initial perturbation is shown at the bottom. (b) Single mode amplitudes. Two postshot calculations are shown. The black line only includes modes less than 100; the red line includes all modes, including the prominent mode 500 structure. Insets show $\kappa\rho$. Analytic growth rates are included in blue. (c) Comparison of interface amplitudes from seeding the perturbation at the interface or at the outer surface.

$\kappa_{DT} \ll \kappa_{abl}$, $\Delta OD_{layered} = \Delta OD_{sym} - \eta_{int}\rho_{abl}\kappa_{abl}$. Therefore, the difference between the two measurements is directly related to the interface amplitude.

Results from the experiment with a perturbation at the interface are shown in Fig. 5(a). The 2.2 $\mu$m amplitude, mode 60 perturbation is shown at the bottom of this figure. In the data, moderate amplitude growth can be observed between the earliest and latest time. The sinusoidal amplitude from the center three waves is shown in Fig. 5(b). Analytic estimates using the previously discussed RT and RT + BP theories are added to Fig. 5(b) (the amplitudes are arbitrarily scaled to compare the growth rate with the data). Here the one-dimensional simulation was used to determine the Atwood number, $A \approx 0.04$, and the acceleration $\ddot{R} \approx -70$ $\mu$m/ns$^2$ during the measurement period. The amplitude growth rate is greater than that predicted by classical RT. Convergence effects, included in the RT + BP model, give good agreement with the earlier-time data. Two two-dimensional HYDRA calculations are also shown here. In the single mode calculation, the initial condition was filtered with a mode 100 low-pass filter. This retains the amplitude of the dominant mode, but misses the higher mode content. In this case, the simulation shows agreement with the earlier-time data but overpredicts the late-time growth. In the "multimode" calculation, the full initial condition information was retained and the simulation was run with mode 1000 resolution. The high-mode structure, coming from the laser ablation process used to create the perturbation, grows quickly and saturates, coupling to lower modes and reducing the observed amplitude at later times. This case shows good agreement with all of the experimental data. In reality this high-mode growth will be three-dimensional and possibly turbulent, so further analysis of this problem with a three-dimensional simulation is necessary. The disagreement between the simulations and the analytic models at $r =$ 500–550 $\mu$m is due to the simulations predicting a compressive wave hitting the interface at this time [note the additional shock at 15.6 ns in Fig. 2(a)]. Since the data suggest the growth rate is closer to the analytic model, this compression may not be present, although both the simulation and the analytic model are within the error bars. Also, these large error bars do not constrain the Atwood number well—a factor of several difference in Atwood number is still consistent with the data. Experiments with smaller wavelength perturbations are needed, which would be more sensitive to the Atwood number. This will be pursued in future experiments.

Interface perturbation growth seeded by ablation front imprint and feedthrough or seeded by an initial interface perturbation is directly compared in Fig. 5(c). Here, in the outersurface perturbation experiment, the interface perturbation growth is computed by $\Delta OD_{symcap} - \Delta OD_{layered}$ and assuming the ablation front growth is the same, as discussed previously. Since the slopes between the two data sets are similar, we can conclude that the exponential growth rates are similar. The ~3× larger modulations measured in the outersurface perturbation experiment (despite their initial amplitude being 6.3× smaller) says that perturbations on the outer surface of the capsule are more of a concern than perturbations initially at the interface at this mode number. The agreement between these experiments and models implies that unexpected perturbation seeds (such as the capsule support "tent" [13]) were the main cause of mixing in early NIF experiments. The dominant perturbation seeded by the tent (mode ~20) is longer in wavelength than the perturbations

analyzed here, but modeling predicts that outersurface perturbations will also dominate the growth at the interface at those lower modes. More work is needed to test these conclusions at higher wave numbers and at higher convergence.

This work was performed under the auspices of the U.S. Department of Energy by Lawrence Livermore National Laboratory under Contract No. DE-AC52-07NA27344.

[1] G. H. Miller, E. I. Moses, and C. R. Wuest, Opt. Eng. (N.Y.) **43**, 2841 (2004).
[2] R. Betti, V. N. Goncharov, R. L. McCrory, P. Sorotokin, and C. P. Verdon, Phys. Plasmas **3**, 2122 (1996).
[3] V. N. Goncharov, R. Betti, R. L. McCrory, P. Sorotokin, and C. P. Verdon, Phys. Plasmas **3**, 1402 (1996).
[4] D. S. Clark, S. W. Haan, B. A. Hammel, J. D. Salmonson, D. A. Callahan, and R. P. J. Town, Phys. Plasmas **17**, 052703 (2010).
[5] B. A. Hammel, S. W. Haan, D. S. Clark, M. J. Edwards, S. H. Langer, M. M. Marinak, M. V. Patel, J. D. Salmonson, and H. A. Scott, High Energy Density Phys. **6**, 171 (2010).
[6] M. J. Edwards *et al.*, Phys. Plasmas **20**, 070501 (2013).
[7] S. P. Regan *et al.*, Phys. Plasmas **19**, 056307 (2012).
[8] T. Ma *et al.*, Phys. Rev. Lett. **111**, 085004 (2013).
[9] O. A. Hurricane *et al.*, Nature (London) **506**, 343 (2014).
[10] D. T. Casey *et al.*, Phys. Rev. Lett. **115**, 105001 (2015).
[11] The presence of oxygen nonuniformities near the surface of the capsule [12] and the perturbation seeded by the thin (15–200 nm) membrane or tent that holds the capsule inside the hohlraum [13–15] have been identified as having a more significant role than previously understood. The perturbation caused by the membrane is now better understood (it seeds a perturbation near mode 20 with variations due to ablator material and tent geometry), but future work is needed to characterize oxygen perturbations.
[12] S. W. Haan, H. Huang, M. A. Johnson, M. Stadermann, S. Baxamusa, S. Bhandarkar, D. S. Clark, V. Smalyuk, and H. F. Robey, Phys. Plasmas **22**, 032708 (2015).
[13] B. A. Hammel, R. Tommasini, D. S. Clark, J. Field, M. Stadermann, and C. Weber, J. Phys. Conf. Ser. **717**, 012021 (2016).
[14] S. R. Nagel *et al.*, Phys. Plasmas **22**, 022704 (2015).
[15] R. Tommasini *et al.*, Phys. Plasmas **22**, 056315 (2015).
[16] K. S. Raman *et al.*, Phys. Plasmas **21**, 072710 (2014).
[17] V. A. Smalyuk *et al.*, Phys. Rev. Lett. **112**, 185003 (2014).
[18] D. T. Casey *et al.*, Phys. Rev. E **90**, 011102 (2014).
[19] A. G. MacPhee, J. L. Peterson, D. T. Casey, D. S. Clark, S. W. Haan, O. S. Jones, O. L. Landen, J. L. Milovich, H. F. Robey, and V. A. Smalyuk, Phys. Plasmas **22**, 080702 (2015).
[20] J. L. Peterson, D. T. Casey, O. A. Hurricane, K. S. Raman, H. F. Robey, and V. A. Smalyuk, Phys. Plasmas **22**, 056309 (2015).
[21] G. A. Kyrala *et al.*, Rev. Sci. Instrum. **81**, 10E316 (2010).
[22] S. W. Haan *et al.*, Phys. Plasmas **18**, 051001 (2011).
[23] B. J. Kozioziemski *et al.*, Fusion Sci. Technol. **59**, 14 (2011).
[24] R. Ishizaki, K. Nishihara, H. Sakagami, and Y. Ueshima, Phys. Rev. E **53**, R5592 (1996).
[25] R. Betti, V. Lobatchev, and R. L. McCrory, Phys. Rev. Lett. **81**, 5560 (1998).
[26] D. P. Smitherman, R. E. Chrien, N. M. Hoffman, and G. R. Magelssen, Phys. Plasmas **6**, 932 (1999).
[27] A. L. Velikovich, J. P. Dahlburg, A. J. Schmitt, J. H. Gardner, L. Phillips, F. L. Cochran, Y. K. Chong, G. Dimonte, and N. Metzler, Phys. Plasmas **7**, 1662 (2000).
[28] A. L. Velikovich, A. J. Schmitt, J. H. Gardner, and N. Metzler, Phys. Plasmas **8**, 592 (2001).
[29] J. O. Kane *et al.*, Phys. Rev. E **63**, 055401 (2001).
[30] Y. Aglitskiy, A. L. Velikovich, M. Karasik, V. Serlin, C. J. Pawley, A. J. Schmitt, S. P. Obenschain, A. N. Mostovych, J. H. Gardner, and N. Metzler, Phys. Plasmas **9**, 2264 (2002).
[31] M. M. Marinak, G. D. Kerbel, N. A. Gentile, O. Jones, D. Munro, S. Pollaine, T. R. Dittrich, and S. W. Haan, Phys. Plasmas **8**, 2275 (2001).
[32] G. I. Bell, Report No. LA-1321 (Los Alamos Scientific Laboratory, 1951).
[33] M. S. Plesset, J. Appl. Phys. **25**, 96 (1954).
[34] M. Lombardini, D. I. Pullin, and D. I. Meiron, J. Fluid Mech. **748**, 85 (2014).
[35] L. Carlson *et al.*, Fusion Sci. Technol. **67**, 762 (2015).
[36] J. L. Peterson, D. S. Clark, L. P. Masse, and L. J. Suter, Phys. Plasmas **21**, 092710 (2014).
[37] These simulations use a similar procedure as other indirect-drive capsule calculations at the NIF [38]. The radiation source is obtained from an integrated calculation that includes the lasers, hohlraum, and capsule. That radiation source is then used in higher resolution capsule-only calculations and adjusted to match shock timing [39], capsule trajectory [40,41], and bang-time [42] measurements from dedicated tuning experiments.
[38] D. S. Clark *et al.*, Phys. Plasmas **20**, 056318 (2013).
[39] H. F. Robey *et al.*, Phys. Plasmas **19**, 042706 (2012).
[40] D. G. Hicks *et al.*, Phys. Plasmas **19**, 122702 (2012).
[41] J. R. Rygg *et al.*, Phys. Rev. Lett. **112**, 195001 (2014).
[42] O. L. Landen *et al.*, Phys. Plasmas **17**, 056301 (2010).